Applied Energy 273 (2020) 115230

Contents lists available at ScienceDirect

Applied Energy

journal homepage: www.elsevier.com/locate/apenergy

Molar-volume asymmetry enabled low-frequency mechanical energy harvesting in electrochemical cells

Weijiang Xue[a,1], Tianwu Chen[b,1], Zhichu Ren[a,1], So Yeon Kim[a], Yuming Chen[a], Pengcheng Zhang[c], Sulin Zhang[b,*], Ju Li[a,*]

[a] Department of Nuclear Science and Engineering and Department of Materials Science and Engineering, Massachusetts Institute of Technology, Cambridge, MA 02139, USA
[b] Department of Engineering Science and Mechanics, The Pennsylvania State University, University Park, PA 16802, USA
[c] Center for Advancing Materials Performance from the Nanoscale, State Key Laboratory for Mechanical Behavior of Materials, Xi'an Jiaotong University, Xi'an 710049, China

HIGHLIGHT

- Thermodynamic framework guided a new molar-volume asymmetry based energy harvester.
- An intercalation-conversion electrode couple was used to prototype this harvester.
- An ideal mechanical-to-electricity conversion efficiency of 19.5%.
- The design strategy sheds more light on low-frequency mechanical energy harvesters.

GRAPHICAL ABSTRACT

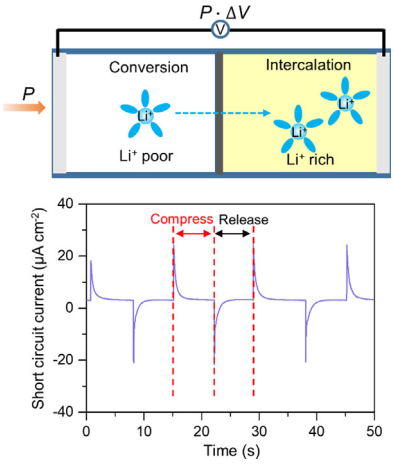

ARTICLE INFO

Keywords:
Energy harvesting
Chemomechanically
Intercalation-conversion electrode couple
Thermodynamic framework

ABSTRACT

In an electrochemical cell, unequal mechanical work due to mass action into the two electrodes can generate chemical potential difference that drives Li^+ flow across the electrolyte, constituting the fundamental basis for electrochemically driven mechanical energy harvesting. The diffusional time scale inherent to the electrochemical setting renders efficient low-frequency energy conversion. From thermodynamic analyses we reveal that there exist two distinct paradigms for electrochemically driven mechanical energy harvesting, enabled by pressure or molar-volume asymmetry of the electrodes. Guided by the thermodynamic framework, we prototype the first molar-volume asymmetry based energy harvester consisting of an intercalation-conversion electrode couple. The harvester can operate under globally uniform pressure and deliver a high power density of ~0.90 μW cm^{-2} with long-term durability. Under an open-circuit condition, the device operates in a novel ratchetting mode under which compression/decompression cycling causes continuous rise in voltage, yielding a blasting power output of ~143.60 μW cm^{-2}. Such a ratchet effect arises due to the chemomechanically induced residual stress in the electrodes during cycling. Compared to the pressure-asymmetry based harvesters, the new

* Corresponding authors.
E-mail addresses: suz10@psu.edu (S. Zhang), liju@mit.edu (J. Li).
[1] These authors contribute equally to the work.

https://doi.org/10.1016/j.apenergy.2020.115230
Received 13 February 2020; Received in revised form 15 May 2020; Accepted 17 May 2020

harvester offers high scalability, processability, safety, and large working area, which make it easy to increase the output power through synchronizing multilayer with large areas. Our device enables mechanical energy harvesting from low-frequency resources, including human daily activities.

1. Introduction

Conversion of mechanical energy to electricity [1] represents an important route to scavenge energy from environment [2], such as human activities, to power mobile consumer electronics and micro/nanosystems [3]. The majority of existing harvesters, including nanogenerators [4] (like polymer-based [5], polydimethylsiloxane-based [6], ZnO-based [7], $BaTiO_3$-based [8], $PbTiO_3$-based [9], ceramic-based [10], composite-based [11] piezoelectric generators [12] and triboelectric generators [13]), electromagnetic [14] and electrostatic energy harvesters [15], have demonstrated high efficiency in collecting high-frequency (> 10 Hz) mechanical energies. In order to collect low-frequency [16] mechanical energies—a dominant frequency range of ambient environmental energy resources, considerable efforts have been undertaken on flexible piezoelectric harvesters [17], frequency-up-conversion based electromagnetic energy harvesters [18], and triboelectric nanogenerators targeted at low frequencies [19]. Inherent to the time scale of ion diffusion across liquid electrolytes, an electrochemical cell converts chemical energy to electricity and vice versa at relatively low frequencies. Aside from electrochemical driving forces in conventional electrochemical cells, unequal mechanical work imparted into the electrodes can also drive ion diffusion across electrolytes, thereby converting mechanical to chemical energies. Such an electrochemical platform embryonates a new class of mechanical energy harvesters at low frequencies [20], complementary to the high-frequency energy generators.

2. Results and discussion

According to the Nernst equation, the open-circuit electronic voltage ΔU generated between two electrodes in an electrochemical cell scales with the chemical potential difference $\Delta\mu_{\mathrm{Li}}$ of the neutral Li atoms: $\Delta U = \Delta\mu_{\mathrm{Li}}/e$. Within each electrode, the chemical potential of Li at given temperature T and pressure P can be generically expressed as $\mu_{\mathrm{Li}} = e_{\mathrm{Li}} - Ts_{\mathrm{Li}} + Pv_{\mathrm{Li}}$, where e_{Li}, s_{Li}, v_{Li} are the partial molar internal energy, entropy, and volume of Li, respectively. The partial molar quantities generally depend on the phase of the electrode material (α) and the local chemical composition $\mathbf{X}^{\alpha}$ of the phase. We define the thermochemical state by the aggregate variables $(\alpha, \mathbf{X}^{\alpha}, T) \equiv \mathbf{C}$, where α takes discrete choices while $\mathbf{X}^{\alpha}$ and T are continuous. This allows us to express $\mu_{\mathrm{Li}}(\mathbf{C}, P) = f_{\mathrm{Li}}(\mathbf{C}) + Pv_{\mathrm{Li}}(\mathbf{C}, P)$, where $f_{\mathrm{Li}} \equiv e_{\mathrm{Li}} - Ts_{\mathrm{Li}}$. Note that $\partial\mu_{\mathrm{Li}}(\mathbf{C}, P)/\partial P|_{\mathbf{C}} = v_{\mathrm{Li}}(\mathbf{C}, P)$, for small but finite P the chemical potential of Li in each electrode can thus be expanded to the leading order:

$$\mu_{\mathrm{Li}}(\mathbf{C}, P) = \mu_{\mathrm{Li}}(\mathbf{C}, 0) + Pv_{\mathrm{Li}}(\mathbf{C}, 0) + \mathcal{O}(P^2) \tag{1}$$

Now consider an electrode couple (denoted by electrodes I and II) at different thermochemical states $\mathbf{C}_{\mathrm{I}}$ and $\mathbf{C}_{\mathrm{II}}$ and under different mechanical pressures P_{I} and P_{II}, respectively. The chemical potential difference of Li across the electrodes is $\Delta\mu_{\mathrm{Li}} \equiv \mu_{\mathrm{Li}}(\mathbf{C}_{\mathrm{II}}, P_{\mathrm{II}}) - \mu_{\mathrm{Li}}(\mathbf{C}_{\mathrm{I}}, P_{\mathrm{I}})$. From Eq. (1), one arrives at:

$$\Delta U \propto \Delta\mu_{\mathrm{Li}} \approx \Delta\mu^{0}_{\mathrm{Li}} + \Delta P v^{\mathrm{II}}_{\mathrm{Li}} + P_{\mathrm{I}}\Delta v^{0}_{\mathrm{Li}} \tag{2}$$

where $v^{\mathrm{II}}_{\mathrm{Li}} \equiv v_{\mathrm{Li}}(\mathbf{C}_{\mathrm{II}}, 0)$, $\Delta P \equiv P_{\mathrm{II}} - P_{\mathrm{I}}$ is the pressure difference, and $\Delta v^{0}_{\mathrm{Li}} \equiv v_{\mathrm{Li}}(\mathbf{C}_{\mathrm{II}}, 0) - v_{\mathrm{Li}}(\mathbf{C}_{\mathrm{I}}, 0)$ is the molar-volume difference across the electrodes. The three terms in Eq. (2) hints different pathways of energy conversion. The first term $\Delta\mu^{0}_{\mathrm{Li}} \equiv \mu_{\mathrm{Li}}(\mathbf{C}_{\mathrm{II}}, 0) - \mu_{\mathrm{Li}}(\mathbf{C}_{\mathrm{I}}, 0)$ depends only on the thermochemical, but not mechanical, differences of the electrodes, where the superscript 0 denotes the pressure-free condition ($P_{\mathrm{I}} = P_{\mathrm{II}} = 0$). This term describes how ideal batteries work. The second and third terms stem from mechanical effects. These two terms correspond to two distinct paradigms for mechanical to electrical energy conversion (Fig. 1), as further elaborated below.

The first paradigm of mechanical-to-electrical energy conversion is based on the pressure difference of the two electrodes, manifested by the second term "$\Delta P v^{\mathrm{II}}_{\mathrm{Li}}$" in Eq. (2). As demonstrated in our previous work [20], in a thin-film like electrochemical cell with two identical conversion-type electrodes (Fig. 1a), v_{Li} is the same across the electrodes so that $\Delta v^{0}_{\mathrm{Li}} = 0$ and the third term $P_{\mathrm{I}}\Delta v^{0}_{\mathrm{Li}}$ vanishes. Bending the thin film generates a pressure difference ($\Delta P \neq 0$) and thus a chemical potential gradient between the electrodes, which drives Li^{+} migration across the electrolyte, enabling mechanical energy harvesting. However, harvesting mechanical energy based on pressure asymmetry presents several drawbacks: (i) Imposing pressure difference is practically limited to bending, and the active volume of the electrode couple is restricted to the bent region, thus limiting the total output current; (ii) Under a pressure gradient, certain regions of the electrodes undergo tensile stress. As tension may lead to material fracture, particularly for ceramics-based electrodes, the pressure asymmetry based design would limit the device life; (iii) Since the electrode must be in contact with the electrolyte, which is often a liquid, a pressure gradient may drive liquid electrolyte flow and thus dissipate additional energy, presenting a source of inefficiency in energy harvesting; (iv) The electrodes and organic electrolyte in this type of harvesters are air-sensitive and toxic [21], which raises serious concerns in safety, cost, and processability.

The second paradigm is based on the molar-volume asymmetry, i.e., the third term "$P_{\mathrm{I}}\Delta v^{0}_{\mathrm{Li}}$" (Fig. 1b). This paradigm can work even under a uniform pressure across the electrodes, i.e., $P_{\mathrm{I}} = P_{\mathrm{II}} = P > 0$ (the second term "$\Delta P v^{\mathrm{II}}_{\mathrm{Li}}$" vanishes). The working efficiency is inherent to the

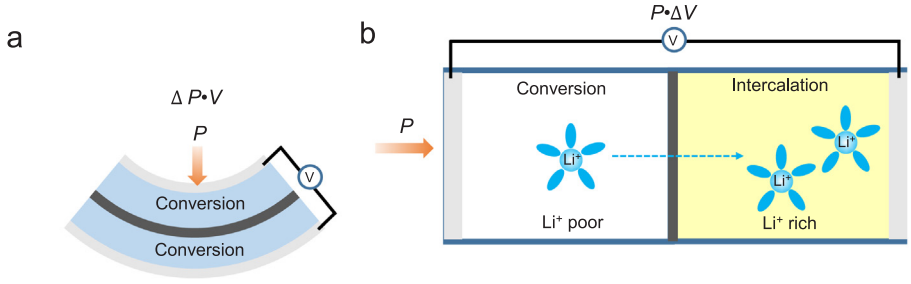

Fig. 1. Two distinct paradigms of electrochemically driven mechanical energy harvesting. (a) The paradigm based on pressure difference ($\Delta P \neq 0$) between two identical conversion-type electrodes ($\Delta v_{\mathrm{Li}} = 0$) with an organic electrolyte[20]. (b) The paradigm based on molar-volume difference ($\Delta v_{\mathrm{Li}} \neq 0$) between an intercalation-type and a conversion-type electrode with an aqueous electrolyte.

differential partial molar volume of Li in different material hosts Δv_{Li}^0. Notably, v_{Li} in an intercalation electrode is significantly smaller than that in a conversion electrode, due to the atomic framework in the former and structural rearrangement in the latter. This molar-volume asymmetry ($\Delta v_{Li}^0 \neq 0$) forms an alternative basis for the mechanical-to-electrical energy harvesting, yet to be explored here. Harvesting energy under this paradigm possesses several advantages over the pressure-asymmetry based harvesters: (i) The harvester is no longer limited by loading modes such as bending or tension, but can work under pressure that is *uniformly* applied to the entire device; (ii) The uniform pressure loading condition facilitates scaling up of the active volume of the electrode couple. Indeed, one can imagine using the liquid electrolyte as a pneumatic fluid to transmit the uniform pressure to everywhere in a bulk device; (iii) The working area is expected to be larger than that of the pressure-asymmetry based counterpart whose working area is restricted to the bent region; (iv) The new harvester can work in an aqueous electrolyte with better processability, safety, non-toxicity, and scalability.

To maximize the voltage output, an effective design strategy is to maximize Δv_{Li}^0 "contrast" between the two electrodes. In this work we rationally select a prelithiated Li-intercalation compound [22], Chevrel-phase $Li_xMo_6S_8$ [23] (α = I), as one electrode, and a prelithiated Li-conversion-type material, Li_yS (α = II), as the other electrode. The compositions x and y can be tuned such that the initial voltage $\Delta U^0 \propto \Delta\mu_{Li}^0 \equiv \mu_{Li}(\mathbf{C}_{II}, 0) - \mu_{Li}(\mathbf{C}_I, 0) = 0$ prior to pressure loading. This can be achieved by shorting using a metal wire connecting the two electrodes for a sufficiently long time. Under this condition, the concentration gradient of Li drives the redistribution of Li between the two electrodes, reaching a chemical equilibrium. We then apply a macroscopically uniform pressure $P_{II} = P_I = P$ on the cell and exploit the molar volume difference Δv_{Li}^0 to drive Li migration across the electrodes. Note that Δv_{Li}^0 vanishes in the pressure-asymmetry based harvester [20] since the electrodes are designed to be thermochemically identical. Thus, the present work explores a completely different paradigm in electrochemically driven energy harvesting.

Our device (Fig. 2a) comprises a $Li_xMo_6S_8$//Li_yS electrode couple separated by a filter paper soaked in an aqueous electrolyte [24] which was prepared by dissolving 21 m (molality, mol-salt in kg-solvent, m for abbreviation) lithium bis(trifluoromethane sulfonyl) imide (LiTFSI) and 7 m lithium triflate (LiOTf) into deionized water. As liquid cannot sustain static shear and is nearly incompressible, the electrolyte has little contribution to the strain energy. The $Li_xMo_6S_8$ and Li_yS electrodes were obtained by electrochemical lithiation of Mo_6S_8 and S_8 electrodes, respectively, using the commercial $LiMn_2O_4$ as the counter electrode. Consistent with previous reports [24], no obvious electrolyte decomposition was observed (Supplementary Fig. S1) during the electrochemical lithiation process, suggesting good electrode/electrolyte compatibility. The cut-off voltage was limited below 2 V to avoid the presence of the short-chain lithium polysulfide [25] which is soluble in the aqueous electrolyte [26]. Due to its non-toxicity, environmental friendliness and low processing cost, the aqueous electrolyte is used here as an auxiliary "pneumatic fluid", allowing much easier scaling up and processing than the toxic and air-sensitive organic electrolytes [27] used in typical batteries.

After heat-treatment at 155 °C for 12 h, the carbon and sulfur formed a uniform mixture (Supplementary Fig. S2). Upon lithiation-delithiation, conversion cathodes [28] (such as S_8) generally undergo much larger volume change [29] than intercalation cathodes (such as Mo_6S_8 or $LiCoO_2$). This is reflected by the different microstructure evolutions, $Mo_6S_8 \rightarrow Li_xMo_6S_8$ for the intercalation electrode and $S_8 \rightarrow Li_yS$ for the conversion electrode (Supplementary Fig. S3). A uniform dispersion of the sulfur, carbon and binder was further confirmed by the energy dispersive spectroscopy (EDS) elemental mapping on the S_8 electrode before and after lithiation (Supplementary Fig. S4). The transition from $Mo_6S_8 \rightarrow Li_4Mo_6S_8$ involves only ~10% volume expansion, indicated by the structural evolution of Mo_6S_8 during lithiation and delithiation by *in-situ* TEM imaging (Fig. 2b). This volume change agrees with an *ab initio* quantum mechanical calculation, $v_{Li}(\mathbf{C}_I, 0) = 6.07$ Å^3. In contrast, S_8 undergoes a large volume change of ~80% upon lithiation [30]. From previous experimental data, we estimated that the $4S_8 \rightarrow 32Li_2S$ transition yields $v_{Li}(\mathbf{C}_{II}, 0) = 10.55$ Å^3. In response to the external pressure, a significant molar volume difference $\Delta v_{Li}^0 \approx 4.48$ Å^3 associated with the intercalation-conversion electrode couple (ICEC) device creates significant chemical potential difference, driving Li^+ flow from the conversion-type electrode to the intercalation-type electrode.

The working principle of the ICEC is illustrated in Fig. 3. To harvest mechanical energy, the device cycles through four states. In the initial state (I in Fig. 3b), an isopotential state in two electrodes is obtained by short-circuiting via an external wire ($A_S = A_M$ in Fig. 3a). Subsequently, applied uniform pressure creates a compressive stress field in the ICEC device, inducing a chemical potential difference between two electrodes (B_S and B_M in Fig. 3a and II in Fig. 3b), driving Li^+ migration from Li_yS to $Li_xMo_6S_8$ until a new equilibrium is reached ($C_S = C_M$ in Fig. 3a, III in Fig. 3b). Meanwhile, electrons flow via external circuit in the same direction as Li^+ migration to maintain charge neutrality, thus generating electrical power. In state IV in Fig. 3b, removing the pressure results in a chemical potential difference between two electrodes (D_S and D_M in Fig. 3a) due to Li concentration gradient, driving reverse Li^+ and e^- flow to attain the original state (I in Fig. 3b).

In considering the energy-conversion efficiency of the ICEC device, we note that the total mechanical energy imparted to the device under a uniaxial and uniform compression P_z is $\Pi_{in} = \frac{1}{2}P_z^2(V_I/E_I + V_{II}/E_{II})$, where V_I and E_I are the volume and Young's modulus of the intercalation electrode, respectively, and V_{II} and E_{II} are those of the conversion electrode. Note that only the hydrostatic part of the stress tensor, $P_h = P_z/3$, contributes to the chemical potential. The working fluid in the cell is assumed to be incompressible and thus stores negligible mechanical energy. When pressurized, the chemical potentials of Li in both the electrodes rise up. The hydrostatic pressure P_h induced chemical potential increase in the intercalation electrode counteracts Li migration. Thus, the fraction of the mechanical work done to the conversion electrode to lift the chemical potential of Li up to the same level ($P_h v_{Li}^I$) as the intercalation side cannot be collected. Corresponding to this level of chemical potential, the conversion electrode is required to reach an intermediate pressure P_h' such that $P_h' v_{Li}^{II} = P_h v_{Li}^I$, and the corresponding uncollectable mechanical energy imparted into is $\frac{1}{2}P_h^2 V_{II}/K_{II}\left(\frac{v_{Li}^I}{v_{Li}^{II}}\right)^2$. The total mechanical energy stored in the active

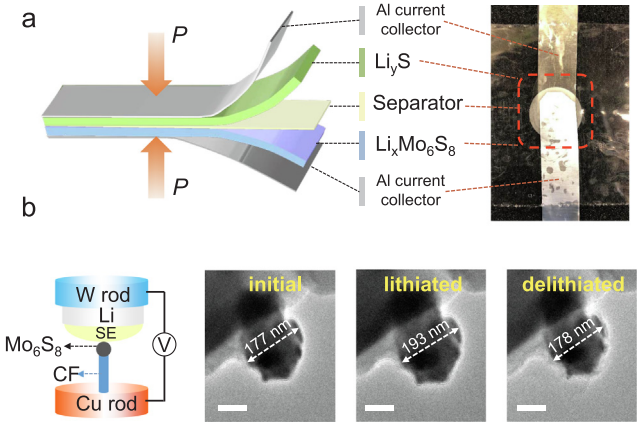

Fig. 2. Characterizations of the ICEC device and the volume change of Mo_6S_8 upon lithium intercalation/deintercalation. (a) Schematic and an optical image of the ICEC device. (b) *In-situ* TEM observation of a Mo_6S_8 nanoparticle under lithiation-delithiation cycle, revealing a much smaller volume change of the intercalation reaction ($Mo_6S_8 \leftrightarrow Li_4Mo_6S_8$) than the conversion reaction $S_8 \leftrightarrow Li_2S$ (~80%). Scale bars, 100 nm.

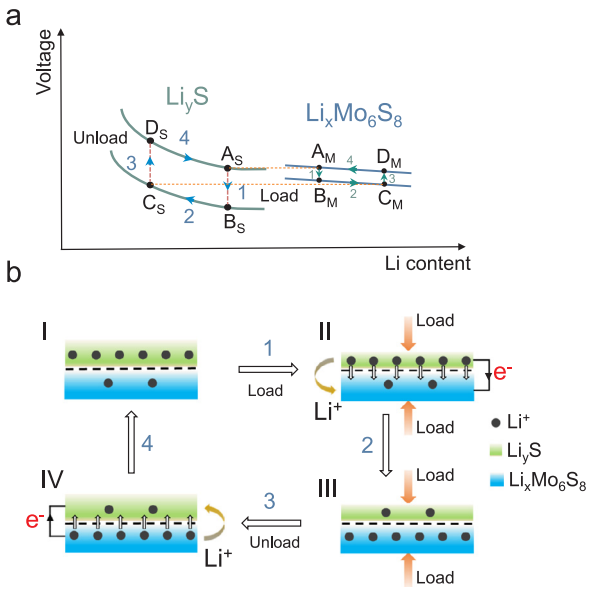

Fig. 3. Working principle of the ICEC device. (a) Four thermodynamic states of the electrodes during a compression-decompression cycle. (b) A schematic view of the compression-decompression cycle. The four states are: I. An isopotential state in the two electrodes is attained by short-circuiting via an external wire. II. Compression on ICEC device induces chemical potential difference of Li between the electrodes, driving Li^+ and e^- migration from Li_yS to $Li_xMo_6S_8$. III. A new isopotential equilibrium is reached. IV. Upon removing the compressive stress, Li^+ and e^- flow back, and the original state I is recovered.

material of the conversion electrode is $\frac{1}{2}P_h^2V_{II}/K_{II}$, giving rise to the output energy: $\Pi_{out} = \frac{1}{2}P_h^2V_{II}/K_{II}\left[1-\left(\frac{v_{Li}^{I}}{v_{Li}^{II}}\right)^2\right]$, where the bulk modulus K relates to the Young's modulus E and Poisson's ratio ν by $K = E/3(1-2\nu)$. The energy conversion efficiency is thus written as

$$\eta \equiv \frac{\Pi_{out}}{\Pi_{In}} = \frac{\rho_E}{\rho_V+\rho_E} f_{II}(1-\rho_{Li}^2) \quad (3)$$

where $\rho_V \equiv V_I/V_{II}$, $\rho_E \equiv E_I/E_{II}$, $\rho_{Li} = v_{Li}^{I}/v_{Li}^{II}$, and $f_{II} = (1-2\nu_{II})/3$ is the constant related to the Poisson's ratio of the conversion electrode. Eq. (3) shows that maximizing the contrast of the molar volumes of Li in the electrode couple (minimizing ρ_{Li}) indeed represents a design strategy to improve the energy-conversion efficiency. In addition, the fact that the energy-conversion efficiency is independent of the working fluid suggests its auxiliary role in perfect pressure transmission without involving extra energy dissipation. For a Poisson's ratio $\nu = 0.25$ and Young's modulus measured by nanoindentation (Supplementary Table S1), the device achieves an energy-conversion efficiency of 19.50% according to Eq (3). It should be pointed out that Eq. (3) suggests multiple strategies improve the device efficiency, including optimizing the ratio of the moduli, etc.

To characterize the performance of the ICEC device, short-circuit current and open-circuit voltage were measured during compression-decompression cycles (Supplementary Fig. S5). As an initial test, the device generated vanishing current when using a pair of two identical electrodes ($Li_xMo_6S_8$//$Li_xMo_6S_8$ or Li_yS//Li_yS) during cyclic compression-decompression (Supplementary Figs. S6 and S7), consistent with the working principle. We optimized the active mass areal loading ratio of $Li_xMo_6S_8$ to Li_yS to a ratio of ~10:1 and the ICEC device exhibited the best output performance (Fig. 4, and Supplementary Figs. S8 and S9). In order to maximize the volume fractions of "active materials" in the electrodes, Li_yS and $Li_xMo_6S_8$ need to be lithiated as much as possible. Otherwise, the output performance was poor if the "x" and "y" are too small, for example, choosing a lower cut-off voltage of ~1.70 V (Supplementary Fig. S10).

We further noted that there existed a background current one order of magnitude lower than the output current, which could be attributed to the slight potential difference between $Li_xMo_6S_8$ and Li_yS electrodes. Such an initial potential difference may arise from the fabrication-induced residual stress/strain in the active materials, elaborated later. It was observed that the background currents had no obvious effect on the energy output (Supplementary Fig. S11). At a loading cycle with an time interval T = 14 s (0.07 Hz), compression induced a sharp rise in the current to a maximum of ~25 μA cm^{-2} (Fig. 4a), demonstrating Li^+ migration under globally uniform pressure. When holding the pressure constant, the short-circuit current gradually decayed since the continuous Li^+ migration led to a concentration gradient that counterbalanced the differential molar volume. The current profile on decompression was symmetric to that on compression, indicative of good reversibility of the device. After relaxation for the same time interval, the two electrodes recovered to their original isopotential states. Our measurement also showed that the output current was proportional to the applied pressure (Fig. 4d), consistent with the linear pressure-chemical potential relationship.

Unlike the conventional electromagnetic generators with dramatic performance decay when the operating frequency drops from 50 to 60 Hz to < 1 Hz [31], the output performance of the ICEC harvester is nearly independent of the loading frequency when operating at the low-freqenncy paradigm. For example, the current output (~20 μA cm^{-2}) at 0.14–0.50 Hz was similar to that at 0.07 Hz (Fig. 4a, b). Moreover, a good scalability is required for a harvester design because a single harvester often cannot provide sufficiently high output. Our ICEC design with the aqueous electrolyte as "working fluid" offers a great potential of scalability since all the components can be easily prepared in the ambient environment compared to the high cost and complicated processing of the harvesters using the toxic and air-sensitive organic electrolyte under atmosphere protection [20]. Fig. 4c shows that the output currents were proportional to the numbers of stacking layers, suggesting easy synchronization of all multiple units to maximize the instantaneous output power. In contrast to the previous pressure-asymmetry based energy harvester [20], the ICEC device has higher energy output because the whole area of the ICEC device is utilized while only part of the area in the bending harvester is active. Thus the ICEC paradigm is demonstrated to be scalable in volume (both height and in-plane). The long-term cycling performance of the ICEC device (Fig. 4d) shows no obvious degradation in the short-circuit current after 300 cycles (Supplementary Fig. S12).

Fig. 5a shows the open-circuit voltage, obtained by monitoring the voltage with and without continuously compressing and decompressing. A background potential of ~30 mV at the initial stage is attributed to the initial potential difference between two electrodes. Upon applying uniform pressure, the open-circuit voltage slightly increased with time and reached ~50 mV. However, unlike the pressure-asymmetry based energy harvester for which the open-circuit voltage can recover its resting potential upon removal of the load, the open-circuit voltage of the ICEC device continuously rose upon cyclic compressing-decompressing (Fig. 5a), exhibiting a ratchet effect. The high voltage obtained by the ratchet effect depends on the loading frequency. For example, for a cyclic loading of compressing for 1 s and decompressing for 30 s, a high value ~130 mV was reached. While ratchetting at a higher frequency (compressing for 1 s - decompressing for 1 s), the open-circuit voltage sharply rose to a higher voltage of ~195 mV. After switching to the short-circuit mode, the ICEC device delivered a very high current of 736.40 μA cm^{-2} (Fig. 5b), which was nearly 40 times of the current by single compression, corresponding to a much higher power output ~143.60 μW cm^{-2}. In contrast, the device without ratchetting only delivered a short-circuit current of 8.50 μA cm^{-2}, two orders of magnitude lower. *In-situ* electrochemical impedance spectroscopy (EIS) was performed to monitor the impedance evolution of the ICEC device at different stress states when keeping the device open-circuited. Under pressure, the charge transfer resistance R_{ct} decreased by nearly fourfold, from ~77.20 Ω in a stress-free state to 22.00 Ω

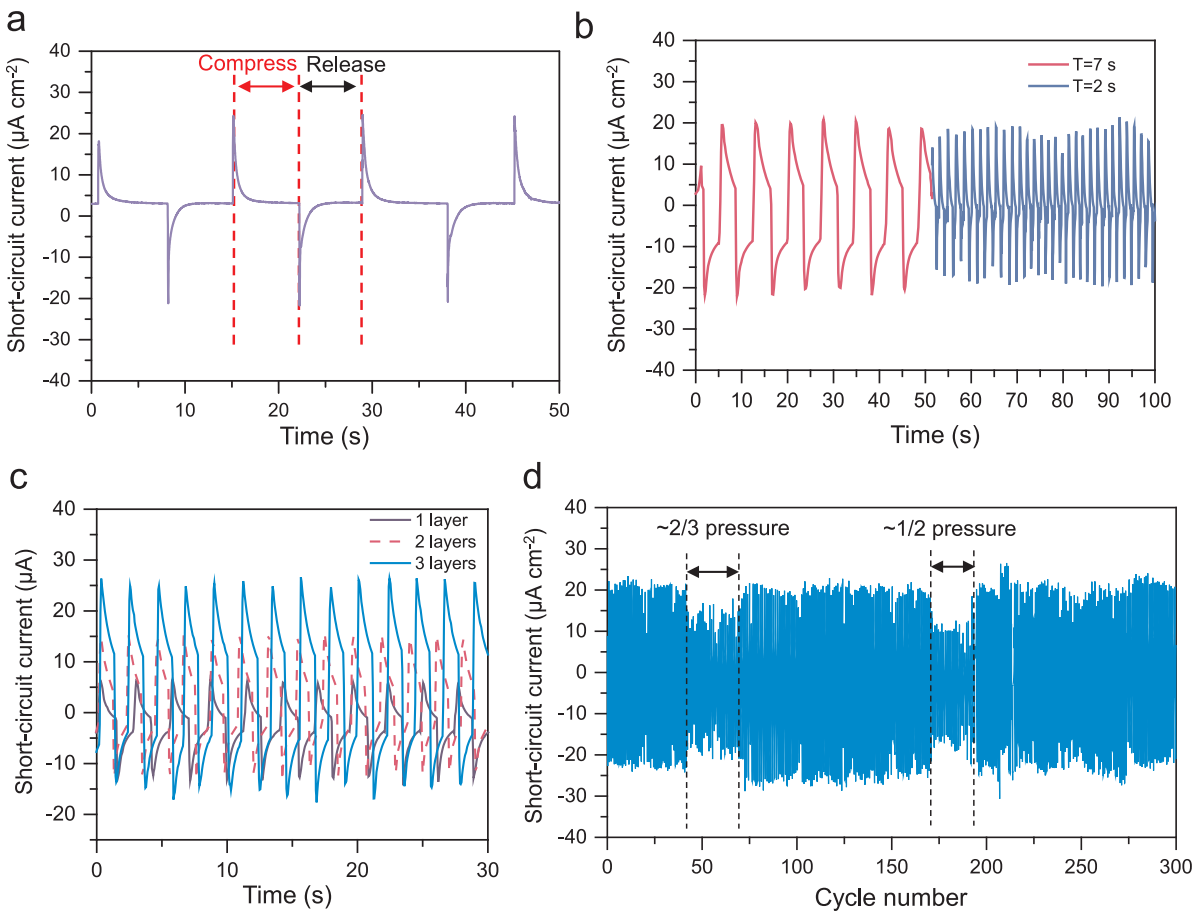

Fig. 4. Short-circuit current output of the ICEC device. (a, b) The measured short-circuit current, obtained by compressing-decompressing cycles, with an applied pressure of ~5 MPa and different time intervals (t = 14 s, 7 s, and 2 s); (c) The measured short-circuit current by stacking multilayers of electrodes with different S_8 loadings (0.4 mg cm^{-2}), demonstrating scaling of the device. The loading ratio between Mo_6S_8 and S_8 in the electrodes is 10:1. (d) Electricity generated during long-term repeated compressing-decompressing cycles, indicating excellent durability.

under 5 MPa compression, which recovered to 44.20 Ω upon releasing the compression (Supplementary Fig. S13). The pressure-dependent charge transfer resistance may be attributed to the better contact between carbon blacks, electrolyte, and Li_yS under pressure.

The ratchet effect indicates residual stress/strain in the active materials upon removal of pressure, which hinges upon the material heterogeneity and chemomechanical loading cycles in the electrodes. Unlike the uniform and dense e-beam deposited Li_xSi electrode [20], the Li_yS electrode is porous, mixed with carbon particles and binders (Supplementary Fig. S14). In the Li_yS electrode, the Li_yS particles are mechanically much softer [22] than the carbon particles and thus prone to plastic yielding under combined applied pressure and chemical insertion/deinsertion of Li, while the carbon particles merely elastically deform. Starting with a stress-free Li_yS electrode, compressive stress is generated in both the Li_yS and carbon particles upon applied pressure (Supplementary Fig. S15a). The compressive stress elevates the chemical potential of Li, driving Li out of the Li_yS electrode. The outward diffusion of Li leaves excess vacancies in the Li_yS particles. As a result, the Li_yS particles are in tension while the carbon particles are still in compression under the applied uniform pressure (Supplementary Fig. S15b). Upon removal of the pressure, both the particles undergo elastic unloading. The overall pressure-free state of the Li_yS electrode indicates that the Li_yS particles is under increased tension, while the carbon particles under reduced compression (Supplementary Fig. S15c). The tensile stress lowers the chemical potential of Li, drawing Li back to the Li_yS particles from the intercalation electrode. Li insertion generates chemical strain into the Li_yS particles. The continuous Li flow switch the stress in the particles (Supplementary Fig. S15d), i.e., from compression to tension in the carbon particles, and tension to compression in the Li_yS particles.

Our modeling results show that the Li_yS particles become in compression before they can recover their original concentration. Our simulations in Fig. 5c further show that the residual stress generated in each cycle monotonically decreases. Thus, the accumulated residual stress over the cycles gradually reaches a plateau beyond which further cycling leads to vanishing increment of the residual stress. Further, due to the large differences in porosity and mechanical properties of Li_yS and $Li_xMo_6S_8$, the chemomechanically induced residual compressive stresses in the $Li_xMo_6S_8$ particles is much smaller than that in the Li_yS particles, corresponding to differential residual compressive stresses, i.e., a finite ΔP. During each loading cycle, ΔP increases, leading to the ratchet effect. Noticeably, in the ratchet mode, the working principle of the ICEC device deviates from the originally designed, pure "$P{\cdot}\Delta v$" paradigm, but operates in a mixed "$P{\cdot}\Delta v$" and "$\Delta P{\cdot}v$ " mode.

The ICEC harvester outperforms, both on the regular and ratchet modes, piezoelectric (PZT) generators (including PZT ribbon [32], PZT ceramics [33] and ZnO nanowires [7]), triboelectric nanogenerators [31], and other generators based on 2D black phosphorus (BP) nanosheets [34] and ionic diodes [35], particularly at low frequency paradigm (Supplementary Table S2). The use of the aqueous electrolyte as the working fluid renders the ICEC harvester unmatched processability, safety and scalability over the pressure-asymmetry based harvesters.

The inherent material heterogeneity of the electrode materials brings in significant challenges for further improving the device efficiency. Heterogeneous material components in electrodes, including

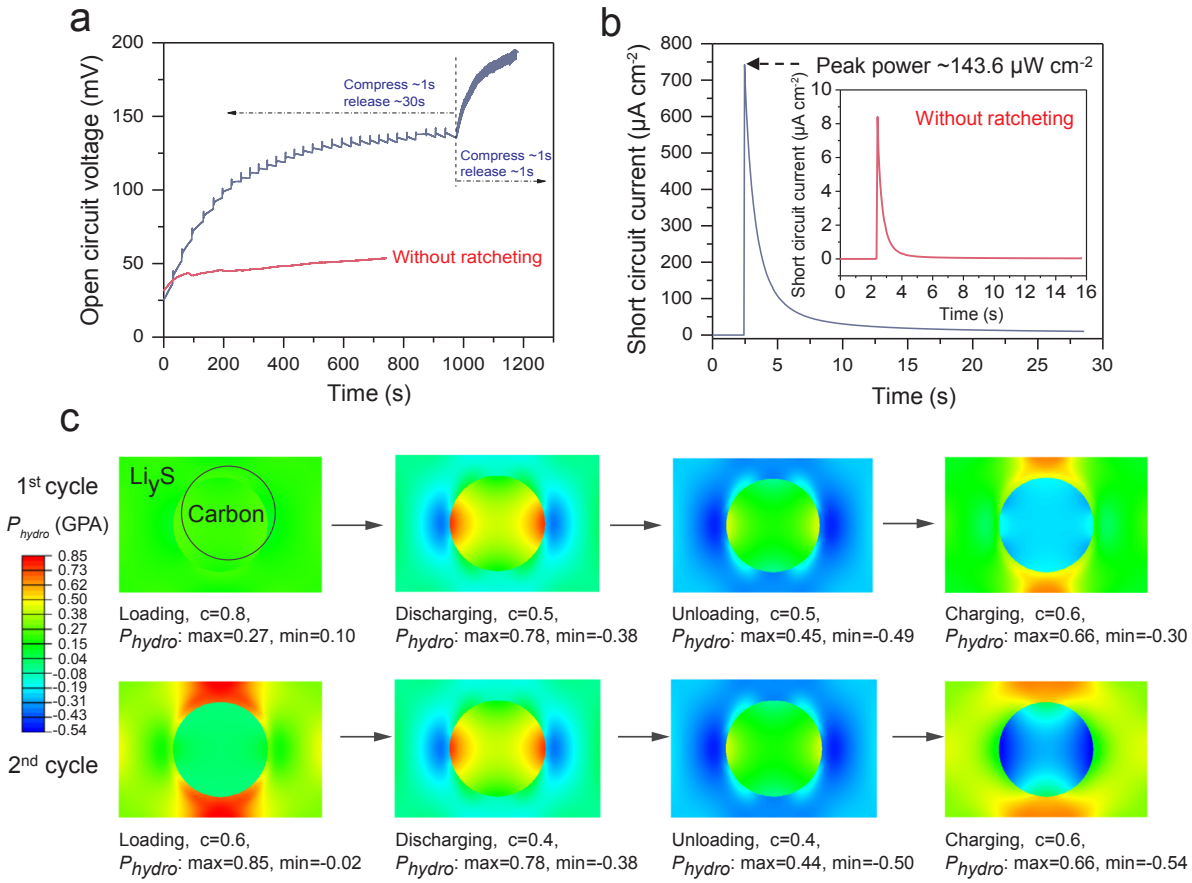

Fig. 5. Blasting power output induced by ratchetting. (a) The open circuit voltage can be ratchetted up to ~195 mV by repeated compression-decompression cycles. (b) After ratchetting, the ICEC device can output a high current of ~736.40 μA cm^{-2}, corresponding to peak power of 143.60 μW cm^{-2}. (c) Chemomechanical simulation of the stress evolution of the conversion electrode during the 1st and 2nd cycles, where P_{hydro} is hydrostatic pressure and c the normalized concentration of Li (c = 0, 1 indicates pure S_8 and Li_2S, respectively).

pores and material interfaces, inevitably dissipate a large amount of mechanical energy, which explains the discrepancy between the experimentally measured and theoretical device efficiencies. Simply eliminating the material heterogeneity may not necessarily improve the efficiency as these internal surfaces and interfaces facilitate fast ion migration. Improving the device performance necessitates balancing these factors in electrode material design. Nevertheless, our experiments demonstrate that the material heterogeneity leads to an unexpected ratchet effect in which the pressure asymmetry and molar-volume asymmetry are simultaneously harnessed.

3. Conclusions

In the present paper, guided by the thermodynamic framework, we have demonstrated an electrochemically driven mechanical energy harvester based on the molar volume asymmetry in an intercalation-conversion electrode couple, in parallel to our previously developed harvester based on pressure asymmetry. Under uniform pressure, the molar volume difference induces chemical potential difference between the two electrodes that drives Li^+ migration, converting mechanical energy to electricity. The harvester delivers a high power density of ~0.90 μW cm^{-2} with good long-term durability. In open-circuit conditions, the device exhibits a novel ratchetting mode causing continuous rise in voltage under compression/decompression cycling, yielding a blasting power output of ~143.60 μW cm^{-2}. Such a ratchet effect arises due to the chemomechanically induced residual stress in the electrodes in each cycle. The thermodynamic framework and the design strategies fill the gap of highly efficient energy harvesters at low-frequency paradigms. Such mechanical energy harvesters may have potential applications in scavenging energies from environment, such as human activities, where low-frequency energy resources dominate.

4. Methods

4.1. Fabrication of the electrodes

Mo_6S_8 was synthesized by a solid-state method according to Ref. [36]. For the Mo_6S_8 electrode, Mo_6S_8, conductive carbon (TIMCAL, Super C65) and polyvinylidene fluoride (PVDF) in weight ratio of 9:0.5:0.5 were dispersed and stirred in NMP for 24 h. Then the slurry was cast onto an aluminum foil using doctor-blade method followed by drying under vacuum overnight at 60 °C. Finally, the dried electrode was rolled and punched into a disk with a diameter of 10 mm. The areal loading of Mo_6S_8 is about 4–20 mg cm^{-2}, which can be controlled by the height of the doctor blade. For the sulfur electrode, commercial sulfur powder (Sigma Aldrich) and conductive carbon in weight ratio of 4:6 were first hand-milled for 30 min and then sealed in a hydrothermal reactor under Ar protection followed by heat treatment at 155 °C for 12 hr [25]. The fabrication process of the sulfur electrodes were also prepared according to the procedures as Mo_6S_8 electrode. The sulfur and carbon contents in the electrode are 54 wt% and 36 wt%, respectively. The areal loading of sulfur is about 0.4–1.2 mg cm^{-2}. Both the Mo_6S_8 and sulfur electrodes were roll-pressed before lithiation. The aqueous electrolyte was prepared by dissolving 21 m (molality, mol-salt in kg-solvent, m for abbreviation) lithium bis(trifluoromethane sulfonyl) imide ($LiN(SO_2CF_3)_2$, LiTFSI) and 7 m lithium triflate ($LiCF_3SO_3$,

LiOTf) into deionized water.

4.2. Electrochemical lithiation

CR2032-type coin cells were assembled using commercial $LiMn_2O_4$ (MTI Corporation) as cathodes, Mo_6S_8/S_8 as anodes and glass fiber as separators with the aqueous electrolyte. Subsequently, the coin cells were galvanostatically charged to ~2.0 V using Landt CT 2001A battery cycler. After the charging process, the $Li_xMo_6S_8$ and Li_yS electrodes were obtained.

4.3. Characterization

Morphologies of the electrodes were characterized by Zeiss Merlin high-resolution SEM. *In-situ* TEM experiment was conducted on JEOL 2010F TEM with a Nanofactory STM/TEM holder [37]. The solid-state nanobattery was built with Li metal, solid-state electrolyte (SE) and the prepared Mo_6S_8 dispersed on carbon nanofibers. EIS measurements were performed on cells using an electrochemical workstation (Gamry Instruments, Reference 3000). A commercial Triboindenter (Hysitron, Inc.) equipped with a diamond Berkovich indenter was used to perform nanoindentation tests to evaluate the Young's modulus of the intercalation and conversion electrodes based on Oliver-Pharr indentation method [38],

$$\frac{1}{E_r} = \frac{1-\nu^2}{E} + \frac{1-\nu_i^2}{E_i} \tag{4}$$

E_r, E, E_i are reduced modulus, Young's modulus of the indented material and the diamond Berkovich indenter. ν and ν_i are Poisson's ratio of the indented material and Berkovich indenter.E_i = 1141 GPa and ν_i = 0.07, ν = 0.25.

4.4. Device assembly and testing

The $Li_xMo_6S_8$ and Li_yS electrodes were placed on top of each other, separated by a filter paper separator with 80–100 μL electrolyte and were then sealed using transparent tape to obtain pouch type batteries (Fig. 2a). The whole process was done in ambient environment without atmosphere protection. The $Li_xMo_6S_8$ and Li_yS electrodes were short-circuited via external wire for at least 4 hr to obtain the same electrochemical potential. Compressing tests were performed by hydraulic crimper (MTI Corporation) under different pressures and loading speeds. The entire device was connected to a digital multimeter (Keysight 34410A) to measure the current and voltage.

4.5. Chemomechanical modeling

We employed a recently developed chemomechanical model to simulate the lithiation/delithiation process in the conversion electrode [39]. In the finite-strain framework, lithiation induced deformation consists of the stretch rates and the spin rates. The total stretch rate is additive of the three components, the chemical ($\dot{\varepsilon}_{ij}^{c}$), elastic ($\dot{\varepsilon}_{ij}^{e}$), and plastic ($\dot{\varepsilon}_{ij}^{p}$) one, $\dot{\varepsilon}_{ij} = \dot{\varepsilon}_{ij}^{c} + \dot{\varepsilon}_{ij}^{e} + \dot{\varepsilon}_{ij}^{p}$. The chemical stretch rate is assumed to be proportional to the increment of the normalized lithium concentration, $\dot{\varepsilon}_{ij}^{c} = \beta\dot{c}\delta_{ij}$, where β is the lithiation induced expansion and $\dot{c}$ the increment of Li concentration. We set that $c = 0$ indicates pure S and $c = 1$ Li_2S. The elastic stretch rate, $\dot{\varepsilon}_{ij}^{e}$, obeys Hooke's law with the stiffness tensor, C_{ijkl}, depending on 2 independent material constants (i.e., Young's modulus E and Poisson's ratio ν). For the intermediate states of charge, the stiffness tensor is assumed to be linearly dependent on lithium concentration, interpolated by those of pure S_8 and Li_2S. The plastic stretch rate, $\dot{\varepsilon}_{ij}^{p}$, obeys the classic J_2-flow rule. Namely, plastic yielding occurs when the equivalent stress, $\sigma_{eq} = (3s_{ij}s_{ij}/2)^{1/2}$, reaches the yield strength. Here $s_{ij} = \sigma_{ij} - \sigma_{kk}\delta_{ij}/3$ is the deviatoric part of Cauchy stress, σ_{ij}, and $\dot{\varepsilon}_{ij}^{p}$ is proportional to s_{ij}. Note that we assume that both chemical and plastic deformations are spin-free. For the carbon particle, we ignore the changes caused by lithiation/delithiation, and assume it deforms elastically. This chemomechanical model is numerically implemented in the finite element package ABAQUS/standard. For pure S_8, we set E_S = 23.3 GPa, while for Li_2S E_{Li_2S} = 77.6 GPa. The Poisson's ratio and yield strength are set to be independent of c, as ν = 0. 25 and Y = 1 GPa. The volumetric change follows the experimental results presented above, as β = 0.8. For the carbon particle, we set E_C = 250 GPa and ν_C = 0.25.

CRediT authorship contribution statement

Weijiang Xue: Conceptualization, Methodology, Formal analysis, Writing - original draft. **Tianwu Chen:** Methodology, Formal analysis, Writing - original draft. **Zhichu Ren:** Methodology, Formal analysis. **So Yeon Kim:** Methodology. **Yuming Chen:** Methodology. **Pengcheng Zhang:** Methodology. **Sulin Zhang:** Conceptualization, Supervision, Funding acquisition, Writing - original draft, Writing - review & editing. **Ju Li:** Conceptualization, Supervision, Funding acquisition, Writing - original draft, Writing - review & editing.

Declaration of Competing Interest

The authors declare that they have no known competing financial interests or personal relationships that could have appeared to influence the work reported in this paper.

Acknowledgement

We acknowledge support by the National Science Foundation of USA (grant No. NSF ECCS-1610806). We also would like to thank Dr. Sangtae Kim at Department of Nuclear Engineering in Hanyang University, Korea for the valuable suggestions.

Appendix A. Supplementary material

Supplementary data to this article can be found online at https://doi.org/10.1016/j.apenergy.2020.115230.

References

[1] Invernizzi F, Dulio S, Patrini M, Guizzetti G, Mustarelli P. Energy harvesting from human motion: materials and techniques. Chem Soc Rev 2016;45:5455–73.
[2] Gholikhani M, Roshani H, Dessouky S, Papagiannakis A. A critical review of roadway energy harvesting technologies. Appl Energy 2020;261:114388.
[3] Zou H-X, Zhao L-C, Gao Q-H, Zuo L, Liu F-R, Tan T, et al. Mechanical modulations for enhancing energy harvesting: Principles, methods and applications. Appl Energy 2019;255:113871.
[4] Wang ZL, Song J. Piezoelectric nanogenerators based on zinc oxide nanowire arrays. Science 2006;312:242–6.
[5] Han M, Wang H, Yang Y, Liang C, Bai W, Yan Z, et al. Three-dimensional piezoelectric polymer microsystems for vibrational energy harvesting, robotic interfaces and biomedical implants. Nat Electron 2019;2:26–35.
[6] Trinh V, Chung C-K. Harvesting mechanical energy, storage, and lighting using a novel PDMS based triboelectric generator with inclined wall arrays and micro-topping structure. Appl Energy 2018;213:353–65.
[7] Hu Y, Lin L, Zhang Y, Wang ZL. Replacing a battery by a nanogenerator with 20 V output. Adv Mater 2012;24:110–4.
[8] Park KI, Lee M, Liu Y, Moon S, Hwang GT, Zhu G, et al. Flexible nanocomposite generator made of $BaTiO_3$ nanoparticles and graphitic carbons. Adv Mater 2012;24(2999–3004):2937.
[9] Lee YB, Han JK, Noothongkaew S, Kim SK, Song W, Myung S, et al. Toward arbitrary-direction energy harvesting through flexible piezoelectric nanogenerators using Perovskite $PbTiO_3$ nanotube arrays. Adv Mater 2017;29.
[10] Zhang G, Zhao P, Zhang X, Han K, Zhao T, Zhang Y, et al. Flexible three-dimensional interconnected piezoelectric ceramic foam based composites for highly efficient concurrent mechanical and thermal energy harvesting. Energy Environ Sci 2018;11:2046–56.
[11] Dudem B, Kim DH, Bharat LK, Yu JS. Highly-flexible piezoelectric nanogenerators with silver nanowires and barium titanate embedded composite films for mechanical energy harvesting. Appl Energy 2018;230:865–74.
[12] Khalili M, Biten AB, Vishwakarma G, Ahmed S, Papagiannakis A. Electro-mechanical characterization of a piezoelectric energy harvester. Appl Energy 2019;253:113585.

[13] Parida K, Kumar V, Jiangxin W, Bhavanasi V, Bendi R, Lee PS. Highly transparent, stretchable, and self-healing ionic-skin triboelectric nanogenerators for energy harvesting and touch applications. Adv Mater 2017;29:1702181.
[14] El-Hami M, Glynne-Jones P, White N, Hill M, Beeby S, James E, et al. Design and fabrication of a new vibration-based electromechanical power generator. Sens Actuators, A 2001;92:335–42.
[15] Moon JK, Jeong J, Lee D, Pak HK. Electrical power generation by mechanically modulating electrical double layers. Nat Commun 2013;4:1487.
[16] Li M, Jing X. Novel tunable broadband piezoelectric harvesters for ultralow-frequency bridge vibration energy harvesting. Appl Energy 2019;255:113829.
[17] Qi Y, Kim J, Nguyen TD, Lisko B, Purohit PK, McAlpine MC. Enhanced piezoelectricity and stretchability in energy harvesting devices fabricated from buckled PZT ribbons. Nano Lett 2011;11:1331–6.
[18] Donelan JM, Li Q, Naing V, Hoffer J, Weber D, Kuo AD. Biomechanical energy harvesting: generating electricity during walking with minimal user effort. Science 2008;319:807–10.
[19] Wu C, Liu R, Wang J, Zi Y, Lin L, Wang ZL. A spring-based resonance coupling for hugely enhancing the performance of triboelectric nanogenerators for harvesting low-frequency vibration energy. Nano Energy 2017;32:287–93.
[20] Kim S, Choi SJ, Zhao K, Yang H, Gobbi G, Zhang S, et al. Electrochemically driven mechanical energy harvesting. Nat Commun 2016;7:10146.
[21] Xue W, Shi Z, Huang M, Feng S, Wang C, Wang F, et al. FSI-inspired solvent and "full fluorosulfonyl" electrolyte for 4 V class lithium-metal batteries. Energy Environ Sci 2020;13:212–20.
[22] Xue W, Shi Z, Suo L, Wang C, Wang Z, Wang H, et al. Intercalation-conversion hybrid cathodes enabling Li-S full-cell architectures with jointly superior gravimetric and volumetric energy densities. Nat Energy 2019;4:374–82.
[23] Xue W, Yu D, Suo L, Wang C, Wang Z, Xu G, et al. Manipulating sulfur mobility enables advanced Li-S batteries. Matter 2019;1:1047–60.
[24] Yang C, Suo L, Borodin O, Wang F, Sun W, Gao T, et al. Unique aqueous Li-ion/sulfur chemistry with high energy density and reversibility. Proc Natl Acad Sci U S A 2017;114:6197–202.
[25] Xue W, Yan Q-B, Xu G, Suo L, Chen Y, Wang C, et al. Double-oxide sulfur host for advanced lithium-sulfur batteries. Nano Energy 2017;38:12–8.
[26] Yun S, Park SH, Yeon JS, Park J, Jana M, Suk J, et al. Materials and device constructions for aqueous lithium-sulfur batteries. Adv Funct Mater 2018;28:1707593.
[27] Suo L, Xue W, Gobet M, Greenbaum SG, Wang C, Chen Y, et al. Fluorine-donating electrolytes enable highly reversible 5-V-class Li metal batteries. Proc Natl Acad Sci U S A 2018;115:1156–61.
[28] Nitta N, Wu F, Lee JT, Yushin G. Li-ion battery materials: present and future. Mater Today 2015;18:252–64.
[29] Liu M, Rong Z, Malik R, Canepa P, Jain A, Ceder G, et al. Spinel compounds as multivalent battery cathodes: a systematic evaluation based on ab initio calculations. Energy Environ Sci 2015;8:964–74.
[30] Manthiram A, Fu Y, Chung SH, Zu C, Su YS. Rechargeable lithium-sulfur batteries. Chem Rev 2014;114:11751–87.
[31] Zi Y, Guo H, Wen Z, Yeh MH, Hu C, Wang ZL. Harvesting low-frequency (< 5 Hz) irregular mechanical energy: a possible killer application of triboelectric nanogenerator. ACS Nano 2016;10:4797–805.
[32] Qi Y, McAlpine MC. Nanotechnology-enabled flexible and biocompatible energy harvesting. Energy Environ Sci 2010;3:1275.
[33] Platt SR, Farritor S, Garvin K, Haider H. The use of piezoelectric ceramics for electric power generation within orthopedic implants. IEEE/ASME Trans Mechatron 2005;10:455–61.
[34] Muralidharan N, Li M, Carter RE, Galioto N, Pint CL. Ultralow frequency electrochemical–mechanical strain energy harvester using 2D black phosphorus nanosheets. ACS Energy Lett 2017;2:1797–803.
[35] Hou Y, Zhou Y, Yang L, Li Q, Zhang Y, Zhu L, et al. Flexible ionic diodes for low-frequency mechanical energy harvesting. Adv Energy Mater 2017;7:1601983.
[36] Suo L, Borodin O, Gao T, Olguin M, Ho J, Fan X, et al. "Water-in-salt" electrolyte enables high-voltage aqueous lithium-ion chemistries. Science 2015;350:938–43.
[37] Kushima A, Qian X, Zhao P, Zhang S, Li J. Ripplocations in van der Waals layers. Nano Lett 2015;15:1302–8.
[38] Oliver WC, Pharr GM. An improved technique for determining hardness and elastic modulus using load and displacement sensing indentation experiments. J Mater Res 1992;7:1564–83.
[39] Ryu J, Chen T, Bok T, Song G, Ma J, Hwang C, et al. Mechanical mismatch-driven rippling in carbon-coated silicon sheets for stress-resilient battery anodes. Nat Commun 2018;9:2924.

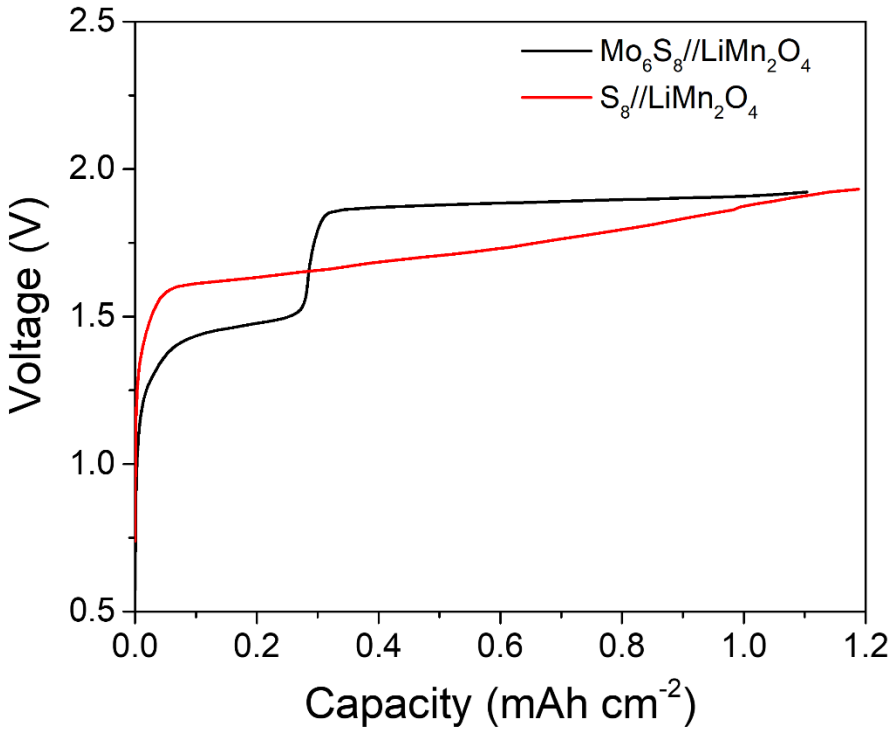

Supplementary Fig. S1. The charging profiles of the coin cells assembled by $LiMn_2O_4$ as cathodes, Mo_6S_8/S_8 as anodes and 21 m LiTFSI in H_2O as electrolyte which were galvanostatically charged to ~2.0 V. After the charging process, the Mo_6S_8 and S_8 were lithiated to $Li_xMo_6S_8$ and Li_yS.

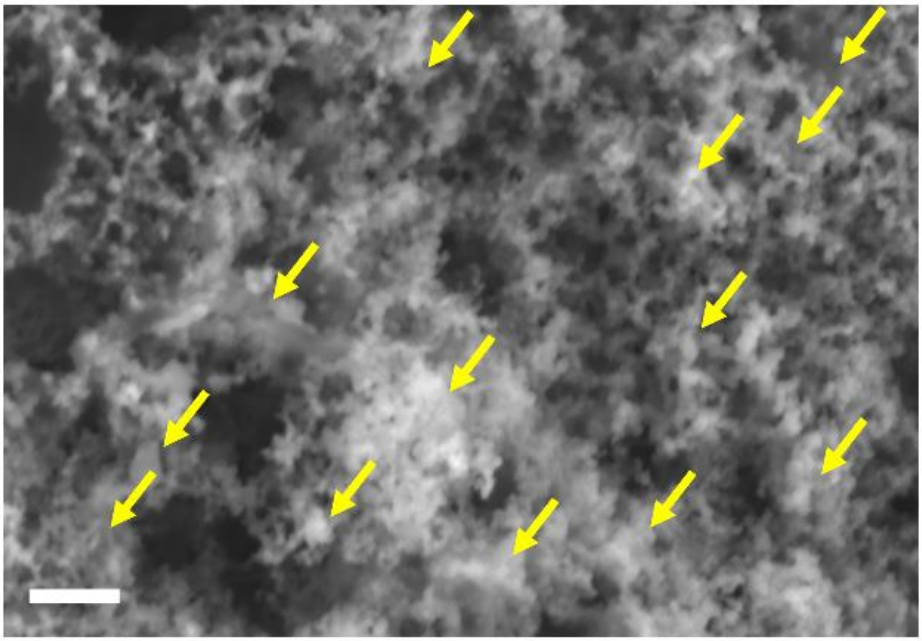

Supplementary Fig. S2 High-resolution SEM figure of the C/S electrode before lithiation. Scale bar 500 nm

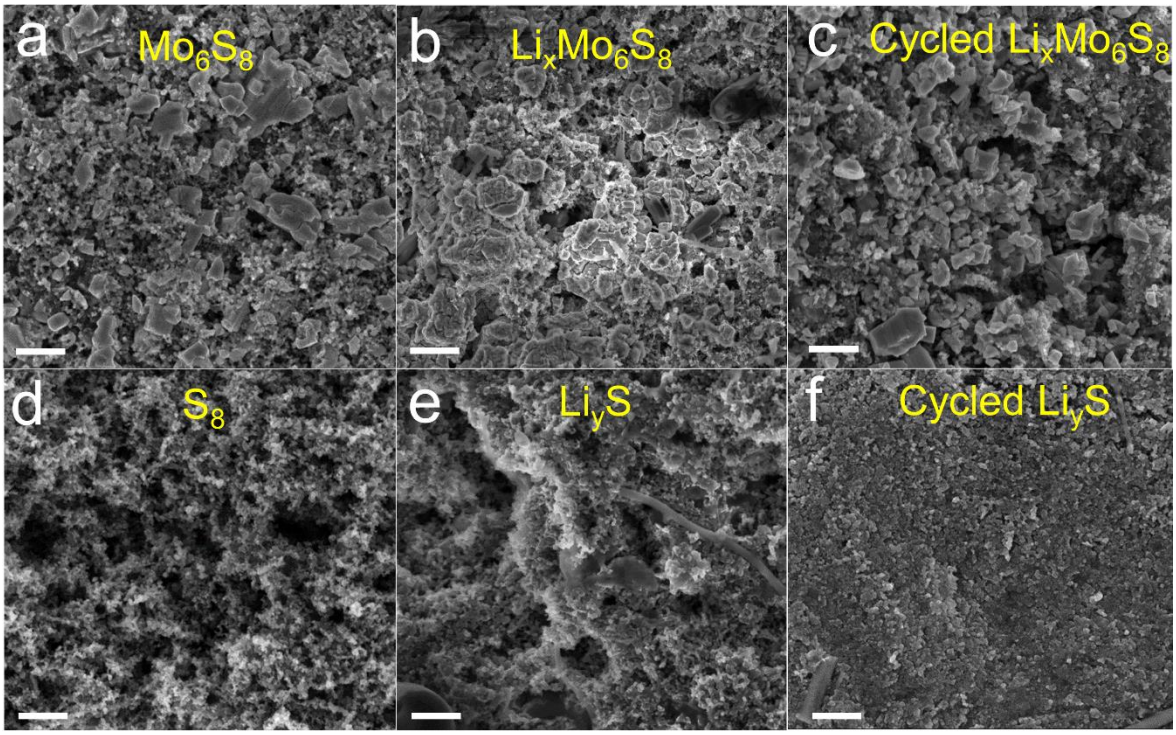

Supplementary Fig. S3. SEM figures of the pristine and lithiated electrodes before and after cycling.
(a) Mo_6S_8 electrode; (b) $Li_xMo_6S_8$ electrode before cycling; (c) $Li_xMo_6S_8$ electrode after cycling
(a) S_8 (C/S_8) electrode; (b) Li_yS electrode before cycling; (c) Li_yS electrode after cycling. The sulfur electrode consists of conductive carbon, S_8 and binder, noted as "S_8 electrode" for short. Scale bars, 1 μm

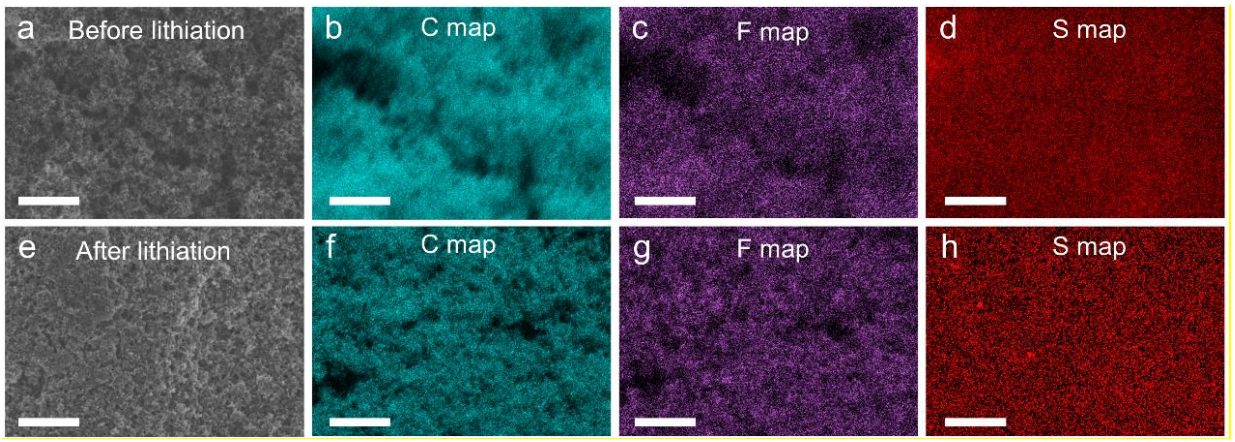

Supplementary Fig. S4 EDS elemental mapping of the sulfur electrode before (a~d) and after (e~h) lithiation. C, F, S maps correspond to conductive carbon, binder (polyvinylidene fluoride, PVDF) and sulfur. Scale bars, 5 μm.

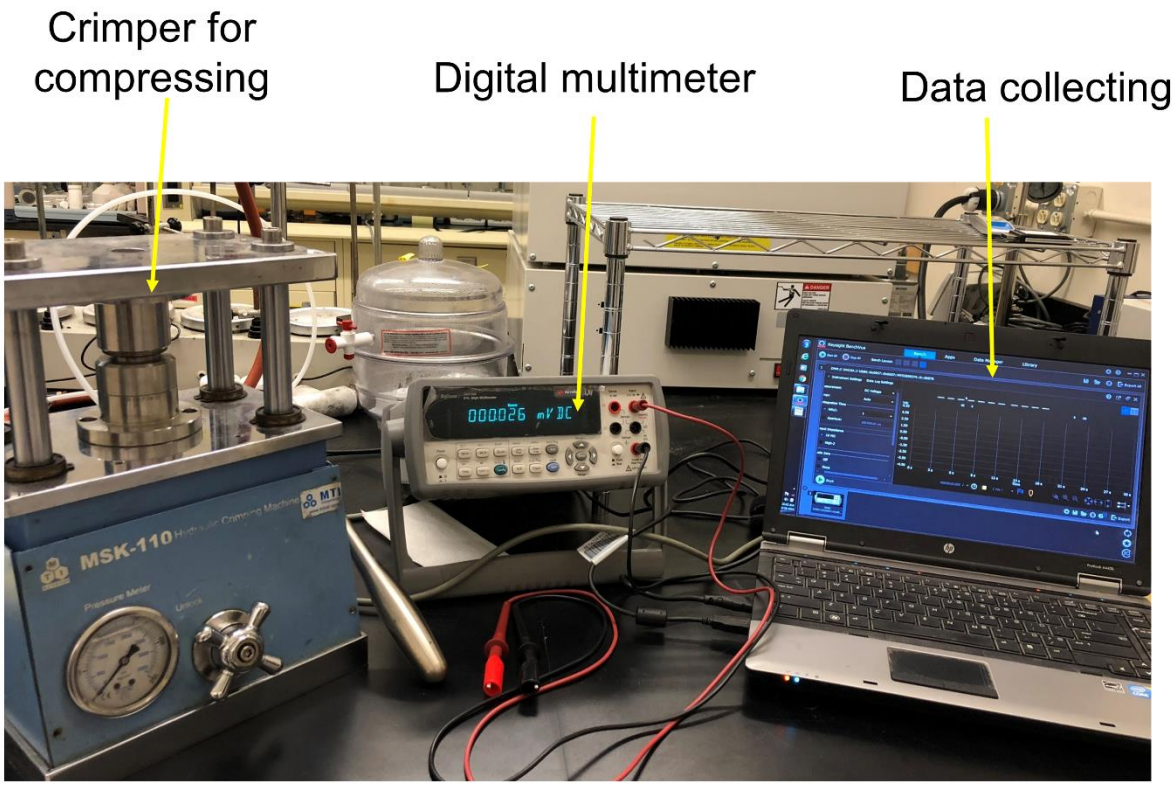

Supplementary Fig. S5. The experimental setups for measuring the outputting electricity during periodically compressing-decompressing the ICEC device

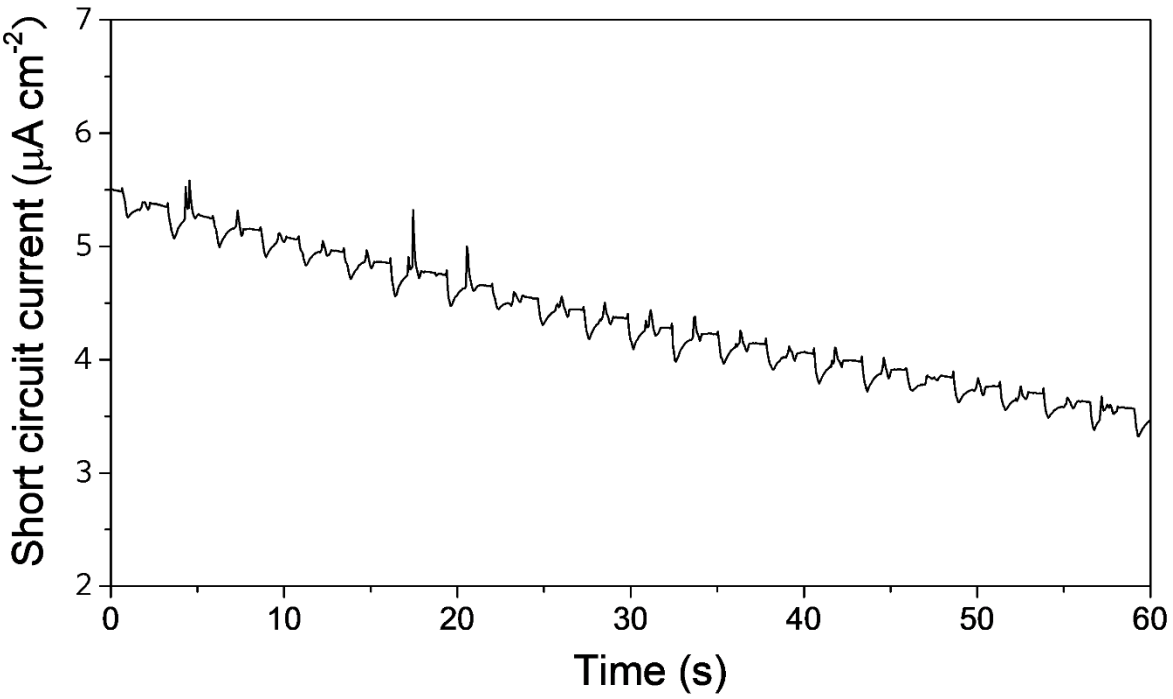

Supplementary Fig. S6. The outputting short circuit current of the device consisting of two identical $Li_xMo_6S_8$ electrodes during cyclic compression-decompression with a pressure~5 MPa

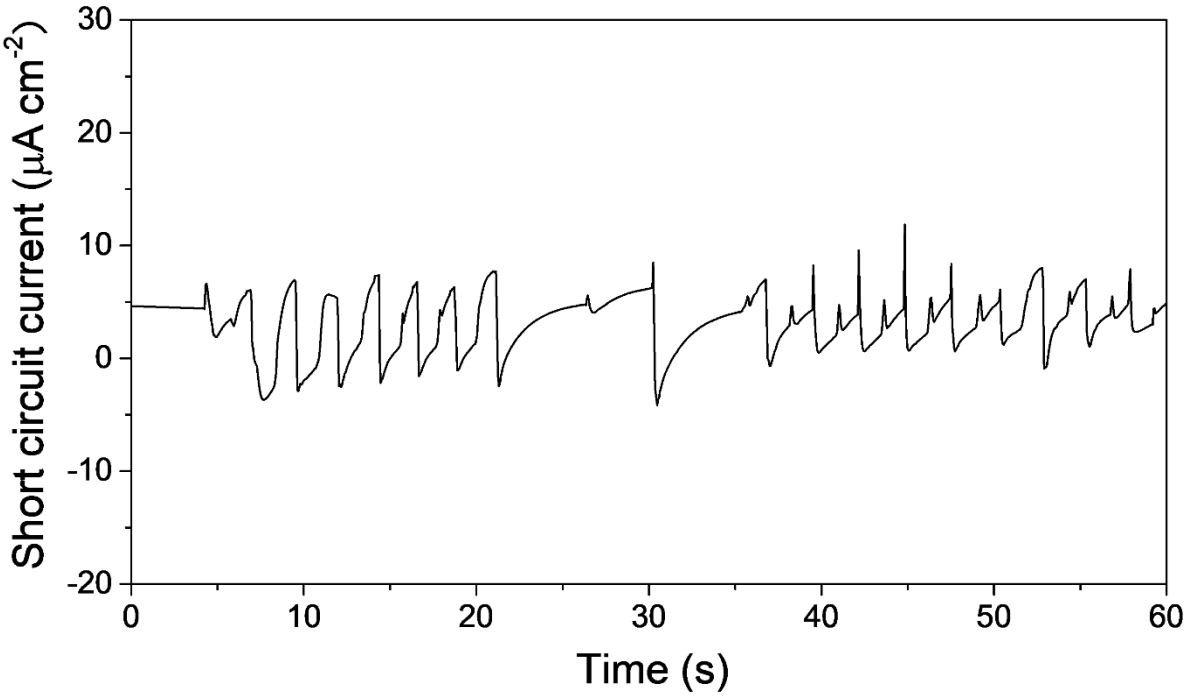

Supplementary Fig. S7. The outputting short circuit current of the device consisting of two identical Li_yS electrodes during cyclic compression-decompression with a pressure~5 MPa

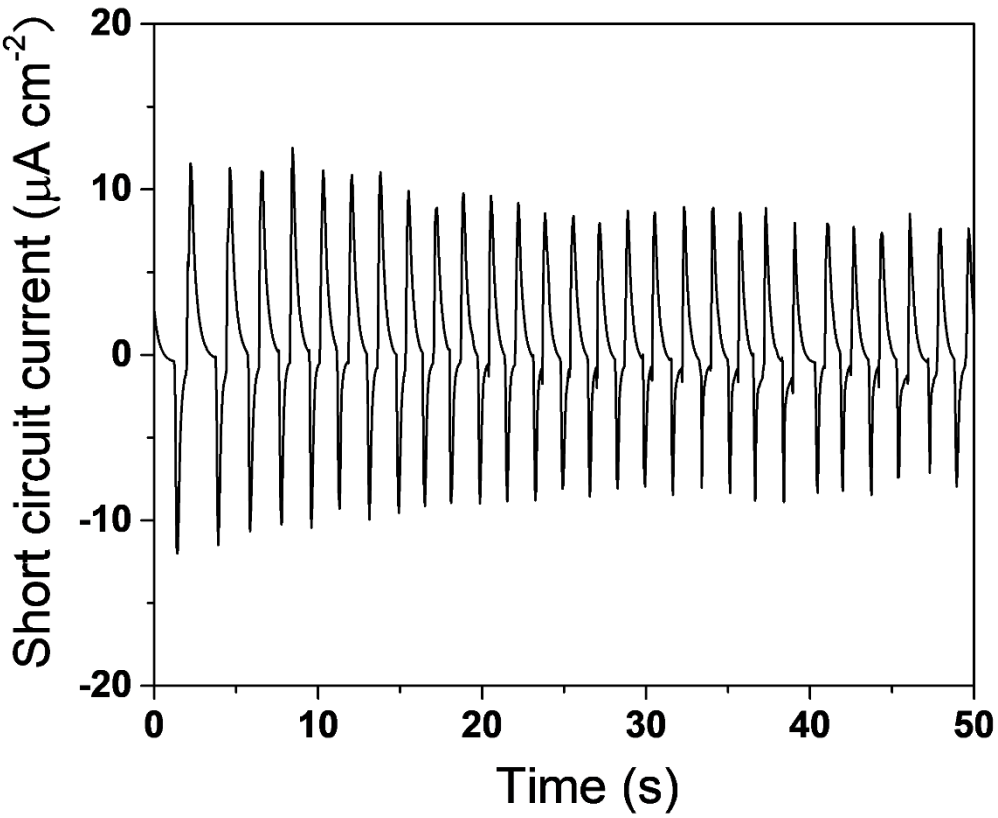

Supplementary Fig. S8. The measured short circuit current of the ICEC device using the areal loading ratio of $Li_xMo_6S_8$: Li_yS=20:1

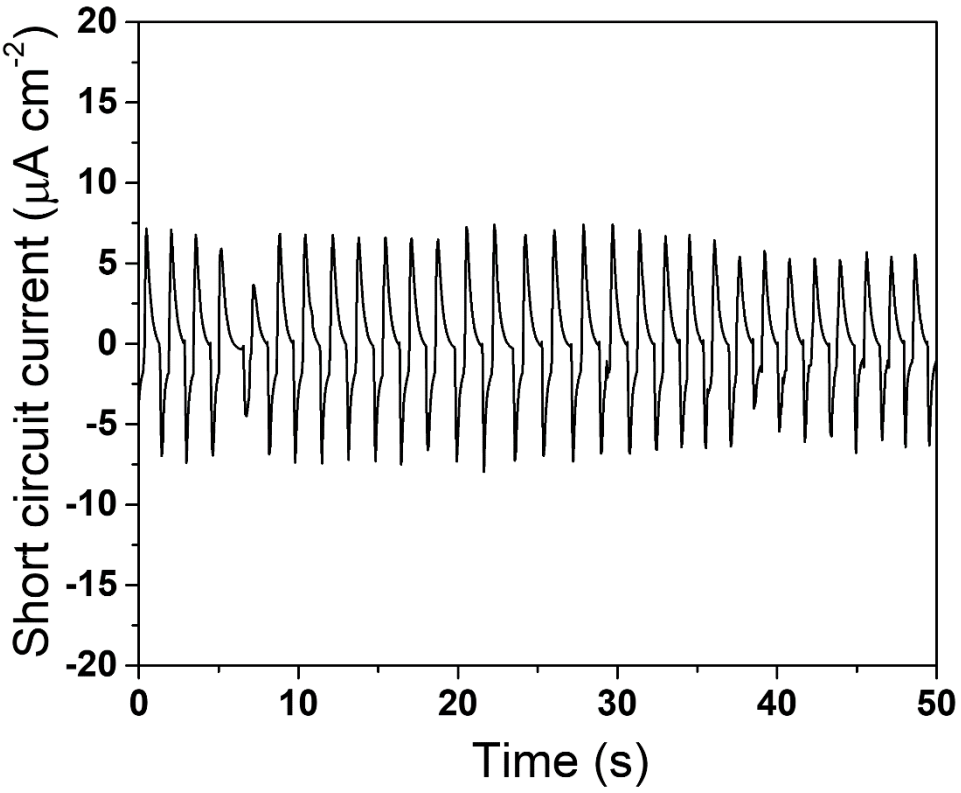

Supplementary Fig. S9. The measured short circuit current of the ICEC device using the areal loading ratio of $Li_xMo_6S_8$:Li_yS=5:1

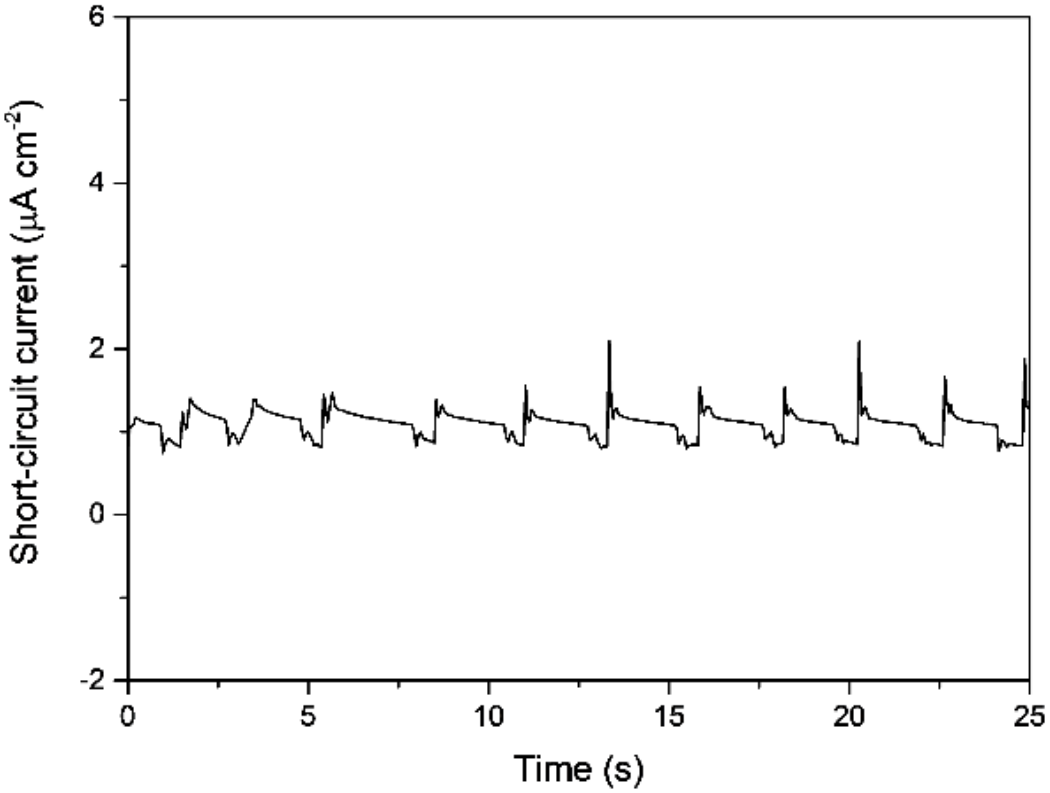

Supplementary Fig. S10. The short-circuit current of the ICEC device composed of Li_yS and $Li_xMo_6S_8$ electrodes lithiated by $LiMn_2O_4$ with cut-off voltage of 1.7 V

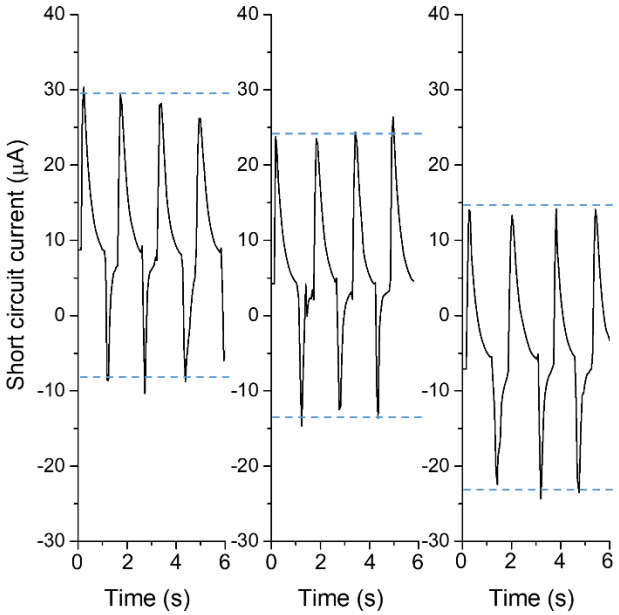

Supplementary Fig. S11 Short circuit currents of ICEC devices with different background currents

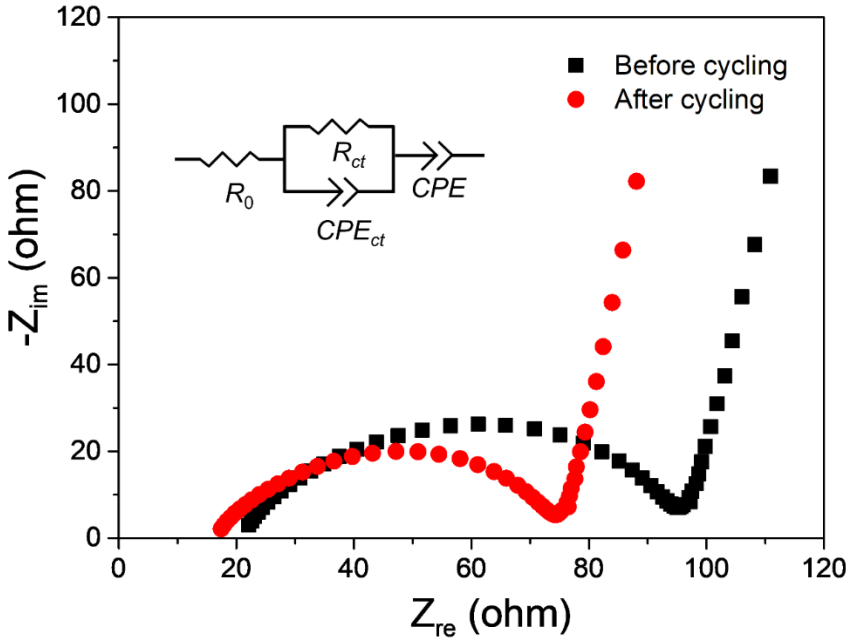

Supplementary Fig. S12. EIS plots of the ICEC device measured before and after cycling

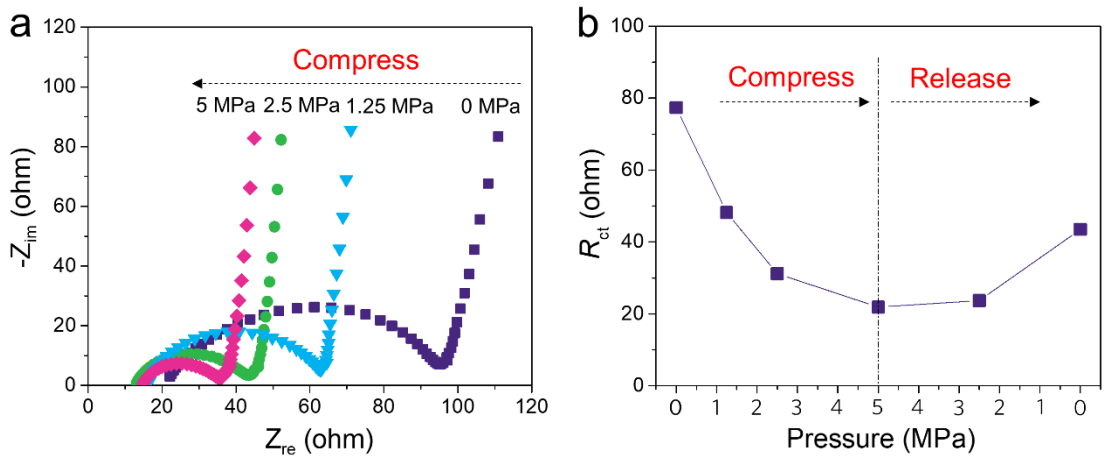

Supplementary Fig. S13. EIS evolution during operation. (a) EIS plots during compressing and releasing; (b) The evolution of charge transfer resistances (R_{ct}) during compressing and releasing.

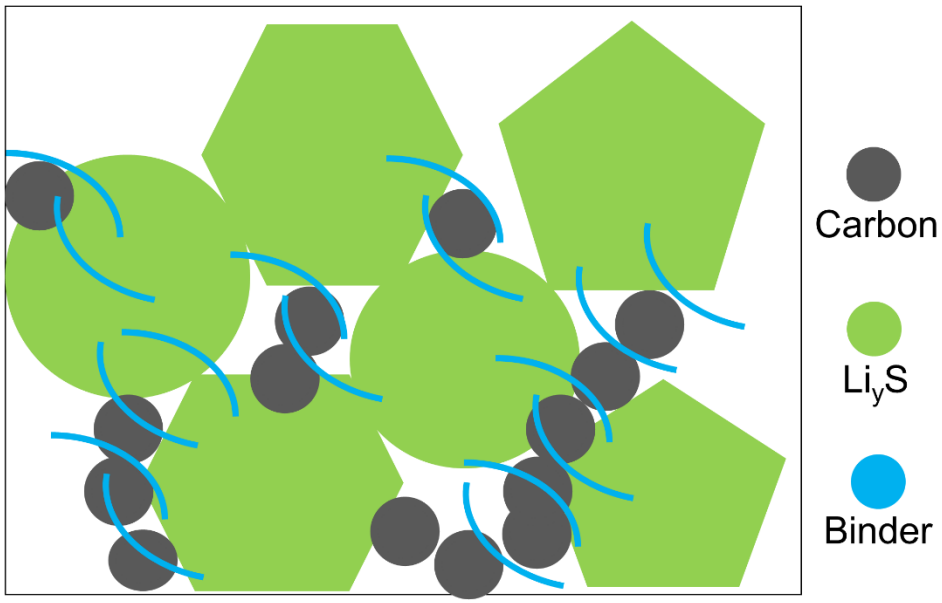

Supplementary Fig. S14. Illustration of the material interface and inhomogeneity inside the conversion electrode, an origin of the residual stress upon compression-decompression cycles

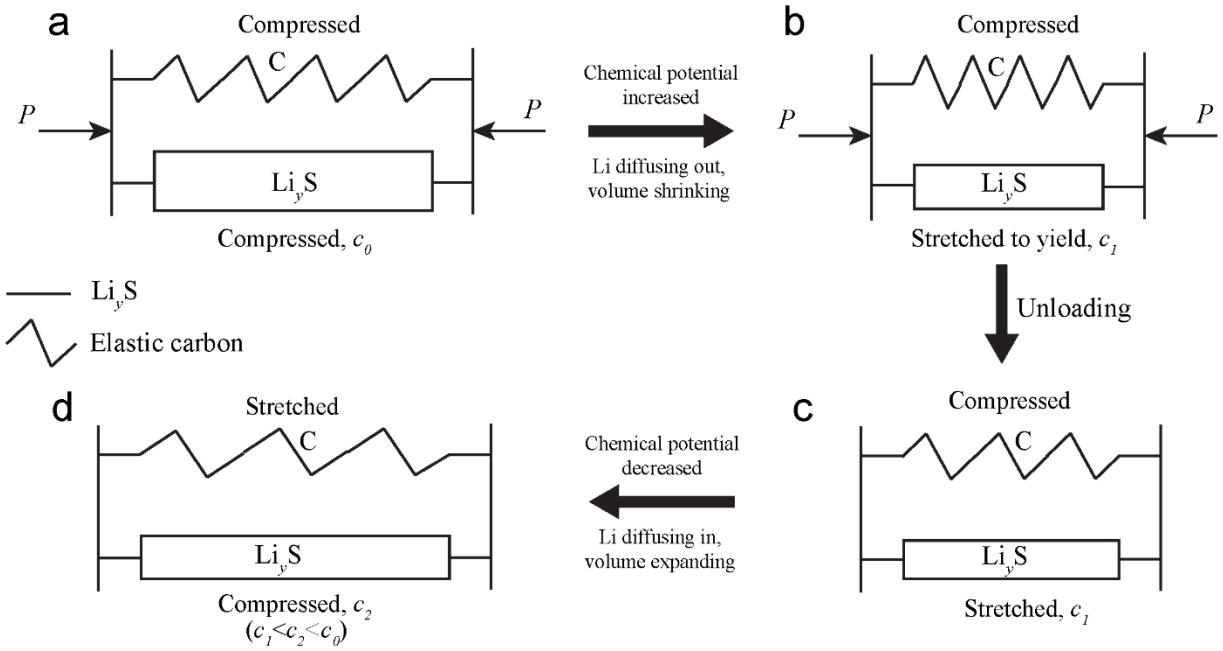

Supplementary Fig. S15. Schematic illustration of the stress states of the Li_yS and carbon particles upon loading and unloading. (a) Compressive stress is generated in both the Li_yS and carbon particles upon applied pressure. (b) The compressive stress elevates the chemical potential of Li, driving Li to diffuse out of the Li_yS electrode. The outward diffusion of Li leads to volumetric shrinkage of Li_yS, altering the stress distribution inside the composite. As a result of force balance, the stress state of Li_yS changes from compression to tension while the carbon particles are further compressed. Since Li_yS is much "softer" than carbon, Li_yS trends to be stretched to yield, which leaves directional permanent deformation inside the Li_yS. (c) Upon removal of the pressure, Li_yS is further stretched plastically, while the carbon particles under reduced compression. (d) The tensile stress lowers the chemical potential of Li, drawing Li back to the Li_yS particles from the intercalation electrode. However, the directional permanent strain in Li_yS does not affect the isotropic volume expansion. Therefore, compressed residual stress appears in Li_yS, increasing the chemical potential to prevent the Li concentration to recover to the original state.

Table S1 Parameters for calculating the efficiency

E_{I}(MPa)	E_{II}(MPa)	K_{I}(MPa)	K_{II}(MPa)	V_{I} (cm^{-3})	V_{II} (cm^{-3})	V'_{II} (cm^{-3})
300±90	64.8±29.1	133.33	28.8	0.003	0.002	0.00078
v_{Li}^{I}(Å^3)	v_{Li}^{II}(Å^3)	ρ_V	ρ_K	ρ_{Li}	f_{II}	
6.07	10.55	1.5	4.63	0.58	0.39	

Volume is calculated based on unit area (cm^2)

Table S2 Comparison of the ICEC device to other types of generators at low-frequency paradigm

		Frequency (Hz)	Peak power (μW cm^{-2})
Our ICEC device	Regular mode	0.07	0.9
		0.14	0.87
		0.5	0.88
	Ratchet mode	0.5	143.6
Pressure-asymmetry based harvester[2]		0.3	0.53
Ionic diodes[3]		0.1	0.0048
2D BP nanosheets[4]		0.1	0.042
Piezoelectric ceramics[5]		1	132.5
PZT ribbon[6]		3.2	0.01
ZnO nanowires[7]		0.6	120
TENG[8]		0.1	0.232

Supplementary references

1. Oliver WC, Pharr GM. An improved technique for determining hardness and elastic modulus using load and displacement sensing indentation experiments. *Journal of materials research* **7**, 1564-1583 (1992).

2. Kim S*, et al.* Electrochemically driven mechanical energy harvesting. *Nat Commun* **7**, 10146 (2016).

3. Hou Y*, et al.* Flexible ionic diodes for low-frequency mechanical energy harvesting. *Adv Energy Mater* **7**, 1601983 (2017).

4. Muralidharan N, Li M, Carter RE, Galioto N, Pint CL. Ultralow frequency electrochemical–mechanical strain energy harvester using 2D black phosphorus nanosheets. *ACS Energy Letters* **2**, 1797-1803 (2017).

5. Platt SR, Farritor S, Garvin K, Haider H. The use of piezoelectric ceramics for electric power generation within orthopedic implants. *IEEE/ASME transactions on mechatronics* **10**, 455-461 (2005).

6. Qi Y, McAlpine MC. Nanotechnology-enabled flexible and biocompatible energy harvesting. *Energy & Environmental Science* **3**, 1275 (2010).

7. Hu Y, Lin L, Zhang Y, Wang ZL. Replacing a battery by a nanogenerator with 20 V output. *Adv Mater* **24**, 110-114 (2012).

8. Zi Y, Guo H, Wen Z, Yeh MH, Hu C, Wang ZL. Harvesting low-frequency (<5 Hz) irregular mechanical energy: a possible killer application of triboelectric nanogenerator. *ACS Nano* **10**, 4797-4805 (2016).